# Affinity and Selectivity of ShK Toxin for the Kv1 Potassium Channels from Free Energy Simulations

M. Harunur Rashid and Serdar Kuyucak*

School of Physics, University of Sydney, New South Wales 2006, Australia

ABSTRACT: The voltage-gated potassium channel Kv1.3 is an attractive target for treatment of autoimmune diseases. ShK toxin from sea anemone is one of the most potent blockers of Kv1.3, and therefore ShK and its analogues have been proposed as therapeutic leads for such diseases. Increasing the selectivity of the proposed leads for Kv1.3 over other Kv1 channels is a major issue in this endeavor. Here we study binding of ShK toxin to Kv1 channels using free energy simulation methods. Homology models for Kv1.1 and Kv1.3 channels are constructed using the crystal structure of Kv1.2. The initial poses for the Kv1.x—ShK complexes are obtained using HADDOCK, which are then refined via molecular dynamics simulations. The binding mode in each complex is characterized by identifying the strongly interacting residues, which compare well with available mutagenesis studies. For each complex, the potential of mean force is calculated from umbrella sampling simulations, and the corresponding absolute binding free energy is determined. The computed binding free energies are in good agreement with the experimental data, which increases the confidence on the model complexes. The insights gained on Kv1.x—ShK binding modes will be valuable in the development of new ShK analogues with better selectivity properties.
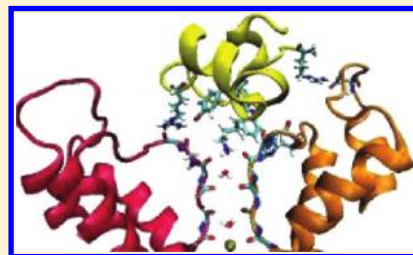
INTRODUCTION

Voltage-gated potassium (Kv) channels play diverse range of roles in cell function from generation of action potential to regulation of calcium signaling and cell volume.[1] Not surprisingly, Kv channels are also implicated in many neurological, cardiovascular, metabolic, and autoimmune diseases,[2] and hence are natural targets for their treatment.[3,4] A basic difficulty in developing drugs targeting Kv channels is that they have similar structures so it is not easy to find a ligand that will selectively bind to a particular Kv channel with high affinity. One needs to exploit small variations in respective structures of Kv channels in order to achieve high selectivity ratios that are essential to avoid undesirable side effects. A case in point is the Kv1.3 channel which is a proven target for treatment of autoimmune diseases.[5−7] Most of the high affinity blockers of Kv1.3 have a similar affinity for Kv1.1 and/or Kv1.2. But Kv1.1 and Kv1.2 are involved in the central nervous system, and should not be targeted by therapeutic drugs—that is actually what most toxins from venomous animals do to kill their preys.

The ShK toxin from the sea anemone *Stichodactyla helianthus*[8,9] is one of the most potent blockers of Kv1.3 with an IC_{50} of 11 pM,[10] and therefore it has been actively pursued for development of an immunosuppressant drug.[11,12] Unfortunately, ShK has a similarly high affinity for Kv1.1,[10] and a great deal of effort has gone into developing analogues of ShK with improved selectivity for Kv1.3 over Kv1.1.[12] Over the past decade, some 380 ShK analogues have been developed for this purpose, with ShK-186[6] and ShK-192[13] having been pursued further as potential drug leads. While docking methods have been utilized in these studies to guide and interpret the experimental results on ShK binding, recent developments in simulations of protein—ligand interactions indicate that much more can be achieved using computational methods.[14−19]

A major hurdle in computational investigation of protein—protein interactions is that, apart from a few cases, the structure of the complex is not known. An optimal method to determine the complex structure is to use a docking program to generate several poses of the complex and then refine them in molecular dynamics (MD) simulations.[14] Convergence of the docking poses to the same complex structure would increase the confidence on the accuracy of the model. Of course, one has to perform further tests on the model by comparing the simulation results to available experimental data such as binding free energies and site-directed mutagenesis data. Feasibility of this approach has been demonstrated on a potassium channel—charybdotoxin complex,[20] where the binding free energy was reproduced accurately using umbrella sampling MD simulations.[21,22] A similar approach has been adapted in two recent computational studies of toxin binding to Kv1.3 channel.[23,24] However, as will be shown below, the Kv1.3 models used in these studies have not been refined properly in MD simulations, leading to wrong complex structures.

Here we perform free energy simulations to investigate the binding of ShK toxin to the Kv1.1, Kv1.2, and Kv1.3 channels. Particular attention is paid to the modeling of the Kv1.3 structure from that of Kv1.2, where the conformation of the mutated His residues near the pore play a critical role in correct docking of toxins. Docking is performed using HADDOCK,[25] which has been shown to be superior to rigid-docking programs in protein docking.[26] The MD-refined Kv1.3—ShK complex is

Table 1. Pore Domain Residues That Differ among the Kv1.x Channels

mKv1.1	E350	E351	A352	E353	H355	S357	S369	Y379	V381
rKv1.2	D352	E353	R354	D355	Q357	P359	S371	V381	T383
mKv1.3	D375	D376	P377	S378	G380	N382	T394	H404	V406

compared with the mutagenesis experiments[27] to confirm that the ShK residues identified as strongly interacting with the Kv1.3 residues are indeed involved in the binding. For each Kv1 channel, the potential of mean force (PMF) for dissociation of ShK is constructed from umbrella sampling MD simulations. The corresponding absolute binding free energies are calculated from the PMFs and compared to the experimental values, which provide a stringent test for the proposed model complexes.

This study is a first step in a computational scheme for finding ShK analogues which have better selectivity properties for Kv1.3 over Kv1.1. The insights gained on Kv1.x–ShK binding modes will be exploited in future work, where the free energy perturbation method will be used to assess whether a particular mutation on ShK improves the Kv1.3/Kv1.1 selectivity. We also hope that the Kv1.x–ShK complex models presented here will spur further experimental activity toward the same goal.

■ METHODS

Modeling of Kv1 Channels. The crystal structure of the mammalian voltage-gated potassium channel Kv1.2 is available[28,29] but not those of Kv1.1 and Kv1.3. As we are interested in binding of ShK toxin to the pore domain of the channel, we consider only the S5–pore–S6 region covered by the residues S308–T421 in Kv1.2. The voltage sensor domain (S1–S4) is not involved in binding of ShK, and the effect of this domain in binding of charydbdotoxin has been shown to be negligible in PMF calculations.[24] The homology between the three Kv1 channels is over 90% in the pore domain, and hence models for Kv1.1 and Kv1.3 can be reliably constructed from the Kv1.2 crystal structure. For this purpose, we use the latter Kv1.2 structure which was obtained in a membrane-like environment (PDB ID 2R9R).[29] Because there is one-to-one correspondence between the pore domain residues, the Kv1.1 and Kv1.3 models are easily constructed from that of the Kv1.2 structure using the mutator plugin in the VMD software.[30]

We have examined the stability of the model channels prior to toxin docking. The simulation system for each channel is constructed using the VMD software following the same protocol. The channel structure is embedded in a lipid bilayer consisting of 125 POPC molecules and solvated with a 0.1 M KCl solution. Extra counterions are included in the system to neutralize it where necessary. Three of the K^+ ions are placed in the selectivity filter and cavity of the channel as observed in the crystal structure.[29] The system is then equilibrated in MD simulations following the protocol we have developed in previous MD simulations of potassium channels.[31,32] Namely, first the protein is fixed and the system is equilibrated with pressure coupling until the correct water and lipid densities are obtained. At that point, the x and y dimensions of the simulation box are fixed and pressure coupling is applied only in the z direction (the box size is about $79 \times 79 \times 80$ Å^3). In the second stage, the restraints on the protein atoms are relaxed gradually by first reducing those on the side chain atoms from $k = 30$ kcal/mol/Å^2 to 0 in 3 ns, and then relaxing the backbone atoms in a similar manner. The resulting system is run for

another 5 ns without restraints to check its stability. The rmsds obtained from the trajectory data show that the channel models remain stable.

The above method works satisfactorily for the Kv1.1 and Kv1.2 channels but the Kv1.3 model appears to be flawed because, unlike the other two cases, it fails to reproduce the available experimental data on ShK binding. Inspection of the differences among the Kv1 channels in the pore domain (Table 1) shows that the most likely culprit is the H404 residue near the pore. Indeed in the initial Kv1.3 homology model, the H404 side chains are observed to make bonds with the D402 side chains in the neighboring monomer. However, these bonds are broken during the relaxation process, and the H404 side chains project out of the pore. Although His is neutral, its side chain is quite bulky and the four of them around the pore prevent a proper docking of ShK. To rectify this situation, we have preserved the H404–D402 cross-links during the relaxation process by introducing restraints, which are lifted after the rest of the protein is relaxed. The Kv1.3 model obtained with this procedure maintains three of the H404–D402 cross-links in a stable configuration in restraint-free MD simulations, and these bonds are retained even after ShK is bound (see Figure 1). Therefore, it has been adapted in the rest of this study. After the umbrella sampling MD simulations of the Kv1.3–ShK system are completed, we have analyzed the 230 ns of trajectory data, and observed that the cross-linking pattern shown in Figure 1 has remained intact throughout the simulations. In previous studies of toxin binding to Kv1.3,[23,24] the H404 side chains have not been modeled properly and project out of the pore, which has prevented a correct docking of the toxins (this point is discussed further in Results and Discussions).

We note that the residues corresponding to H404 are Y379 in Kv1.1 and V381 in Kv1.2. Thus, there is no possibility of cross-linking in Kv1.2. This may be feasible in Kv1.1 with the Tyr side chains but inspection of the Kv1.1 simulations shows no hint of a Y379–D375 cross-link at any stage—presumably the Tyr side chains are too bulky to be embedded around the filter. Interestingly, a similar cross-linking is also observed between T449–D447 in drosophila Shaker channel, strengthening the above argument that the Tyr side chains are too bulky to fit around the filter.

Modeling of Kv1–ShK Complexes. The structure of ShK was determined from NMR (PDB ID 1ROO).[34] It is a 35-residue peptide with the sequence RSCIDTIPKS RCTAFQCKHS MKYRLSFCRK TCGTC, containing four Arg, four Lys, and one Asp residues. Besides the three disulfide bonds between C3–C35, C12–C28, and C17–C32, ShK has three other bonds which confer an extraordinary stability to its structure. These are a salt bridge between D5–K30, a carbonyl oxygen–side-chain coupling between K18–R24 and a backbone H-bond between T6–F27 (Figure 2). The average N–O distances for the three bonds, obtained from 5 ns MD simulations of ShK in bulk are 2.9, 2.7, and 4.1 Å, respectively. Thanks to these bonds, ShK preserves its shape during the umbrella sampling PMF calculations. As a contrast, we note that charybdotoxin is grossly distorted during umbrella
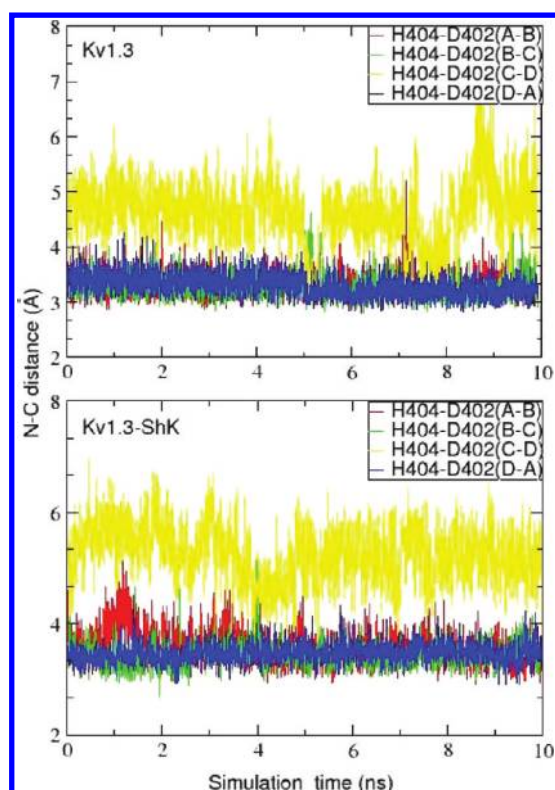
Figure 1. Cross-linking between the H404−D402 residues in Kv1.3. Because the D side chain often flips, the N−C$_\gamma$ distances are shown instead of N−O. The top figure shows these distances in Kv1.3 and the bottom one in the Kv1.3−ShK complex. In three out of four cases, H404−D402 residues remain cross-linked via a strong charge−dipole interaction throughout the simulations (the average N−O distance is 2.7 Å). This coupling is weaker in the case of H404(C)−D402(D) (the N−O distance becomes 4−5 Å), but their side chains still remain near the protein. Comparison of the two figures shows that binding of ShK has a negligible effect on the H404−D402 cross-linking.

sampling simulations,[21] and one has to use restraints in order to obtain correct binding free energies from PMF calculations.[22]
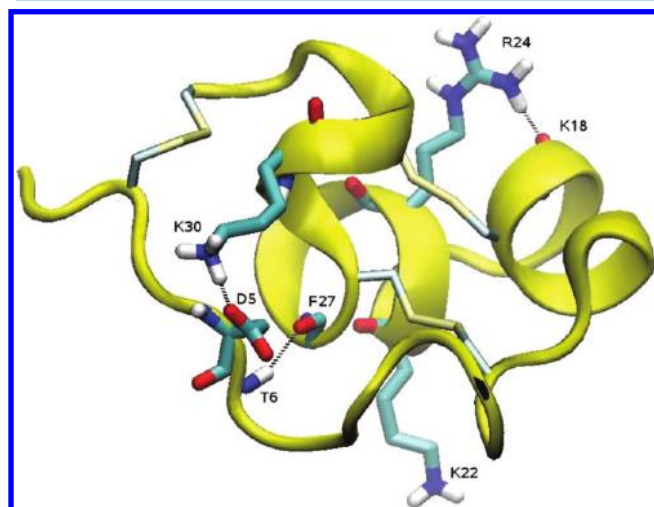
Figure 2. NMR structure of ShK oriented with the pore inserting lysine (K22) pointing downward. Three disulfide bridges between C3−C35, C12−C28, and C17−C32, as well as the bonds between D5−K30, K18−R24, and T6−F27, are indicated explicitly.

The initial Kv1.x−ShK complexes are obtained using HADDOCK protein−protein docking program,[25,26] which has given very good results for docking of toxins to potassium channels.[33] The side chains of the surface residues on the channel (e.g., 350−361 and 376−385 in Kv1.2) as well as the whole ShK peptide are treated as flexible. Because the insertion of the K22 side chain into the filter has been well established experimentally,[10] we use proximity of the K22 side chain to the filter (specifically the last G in the TVGYG sequence) as a restraint in the docking calculations. One thousand conformations are generated for each complex, and the top hundred from scoring are selected for further consideration. Using the K22−filter proximity and the available mutagenesis data, we select the best pose for refinement in MD simulations. We note that in a plot of energy score versus K22−filter distance, a number of candidates are closely clustered at the energy minimum and any of those could have been chosen for refinement.

Following the protocols described above, simulation systems are constructed for each of the Kv1.x−ShK complexes obtained from docking. The channel and toxin atoms are relaxed simultaneously but this is done more slowly—spending 5 ns for each stage instead of 3 ns. The relaxed systems are run for another 5 ns to check for equilibration, and all systems are found to be already equilibrated. The trajectory data are, therefore, used for analysis of the complex structures. The relatively fast equilibration of the Kv1.x−ShK complexes may come as a surprise. To find the reason, we compare the docking results with the complex structures obtained from MD refinement. For all three channels, the average distance of the center of mass (COM) of ShK from the channel COM along the z axis is 26.8 Å (the channel axis coincides with the z axis). The HADDOCK results for the same quantity are 27.4 (Kv1.1), 26.9 (Kv1.2), and 27.1 Å (Kv1.3), which are very close to that of MD. A more detailed comparison showing the atom−atom distances between the strongly interacting residues is presented in Table 2. Again, most of the pair distances are predicted fairly accurately by HADDOCK, and only a few side chains have apparently wrong conformations (i.e., >3 Å difference). Overall, HADDOCK has done an excellent job in providing initial poses that are very close to the final complex structures, which explains the fast equilibration of the systems in MD simulations. (Accuracy of the final complex structures will be discussed in the results section.) We stress that initial poses obtained from rigid docking programs are not as good, which necessitates longer equilibration times in MD simulations.[35]

MD Simulations and Umbrella Sampling. The MD simulations are performed using the package NAMD[36] with the CHARMM22 force field[37] including the CMAP correction.[38] An NpT ensemble is used with the temperature and pressure maintained at 300 K and 1 atm, respectively, via Langevin coupling with damping coefficients of 5 ps^{-1}. Periodic boundary conditions are employed, and the long distance electrostatic interactions are computed using the particle-mesh Ewald algorithm. Lennard-Jones interactions are switched off within a distance of 10−13.5 Å, and the list of nonbonded interactions is truncated at 13.5 Å. A time step of 2 fs is used in all simulations, and the trajectory data is written at 1 ps intervals. In umbrella sampling simulations, the reaction coordinate (Kv1.x-COM to ShK-COM distance along the z axis) is written at every time step.

Table 2. List of the Strongly Interacting Residues in the Kv1.x–ShK Complexes[a]

	ShK	dock	MD av
Kv1.1			
E353–O$_2$(D)	R29–N$_2$	6.0	2.5 ± 0.3
E353–O$_2$(C)	K18–N$_1$	2.6	2.7 ± 0.2
D361–O$_2$(B)	R11–N$_2$	8.1	5.5 ± 0.5
Y375–O(ABC)	K22–N$_1$	3.0	2.7 ± 0.2
Y379–C$_{\varepsilon 1}$(A)	F27–C$_{\varepsilon 2}$	4.0	3.6 ± 0.2
Y379–O$_H$(B)	S20–O$_H$	3.5	3.0 ± 0.3
Kv1.2			
D355–O$_1$(A)	R29–N$_1$	2.6	2.7 ± 0.2
D353–O$_2$(B)	S10–O$_H$	5.9	2.8 ± 0.3
Y377–O(ABC)	K22–N$_1$	3.1	2.7 ± 0.3
D379–O(D)	M21–N	3.3	3.1 ± 0.2
V381–C$_{\gamma 2}$(D)	M21–C$_\gamma$	4.6	3.8 ± 0.3
Kv1.3			
D376–O$_1$(C)	R1–N$_1$	5.0	4.5 ± 0.4
S378–O(B)	H19–N	3.2	3.0 ± 0.5
Y400–O(ABD)	K22–N$_1$	2.9	2.7 ± 0.2
G401–O(B)	S20–O$_H$	2.9	2.7 ± 0.2
G401–O(A)	Y23–O$_H$	3.5	3.5 ± 0.3
D402–O(A)	R11–N$_2$	3.2	3.5 ± 0.3
H404–C$_\gamma$(C)	F27–C$_{\varepsilon 1}$	9.7	3.6 ± 0.2
V406–C$_{\gamma 1}$(B)	M21–C$_\varepsilon$	9.4	4.7 ± 0.3
D376–O$_1$(C)	R29–N$_1$	12.2	10.2 ± 0.3

[a]The average atom–atom distances obtained from HADDOCK and MD simulations are given in the third and fourth columns (in units of Å). The N–O distances are shown for the charge interactions and the closest C–C distance for the hydrophobic ones. Bare C, N, and O refer to the backbone atoms and the subscripted ones refer to the side-chain atoms. The monomer identity is given in parentheses. For the filter Y residues, the average of the three N–O distances is given.

Umbrella sampling simulations follow closely the protocols established in our earlier work on dissociation of charybdotoxin from a KcsA channel surrogate.[21,22] Starting from the complex structure, umbrella windows are generated at 0.5 Å intervals along the channel axis using steered MD simulations. For this purpose, a harmonic force with $k = 30$ kcal/mol/Å^2 is applied to the COM of the ShK backbone atoms, which is pulled at a constant speed of 5 Å/ns for 0.1 ns. After each pulling step, ShK is equilibrated at the window position for 0.3 ns with the same restraining force to relax the effect of steering on the environment. Initial PMFs are constructed up to a distance of 15 Å from the binding site, which is extended further when necessary (i.e., until the PMF becomes flat, signaling that the bulk region has been reached). When insufficient overlap occurs between the adjoining window samples, an extra window is included in the middle of the two windows. Each window is simulated using the same force constant of 30 kcal/mol/Å^2. The reaction coordinates of ShK collected during the umbrella sampling simulations are used in constructing its PMF via the weighted histogram analysis method.[39] Simulations are continued until the convergence of the PMFs is established using various criteria.

To make contact with experiments, the binding constant of ShK needs to be determined. In order to enable such a calculation, we invoke a 1-D approximation and integrate the PMF, $W(z)$, along the z axis

$$K_{eq} = \pi R^2 \int_{z_1}^{z_2} e^{-W(z)/k_B T}\, dz \qquad (1)$$

Here the integration limits are chosen such that z_1 is in the binding pocket and z_2 is in the bulk region where W vanishes. The radius R in the factor πR^2 measures the average cross-sectional area of the binding pocket as explored by the COM of ShK (the reaction coordinate), and it is determined from the transverse fluctuations of the COM of ShK in the binding pocket. It has been shown previously that allowing R to vary with z gives essentially the same answer,[22] and therefore it has not been attempted here. The values of R obtained from restraint-free MD simulations of the complexes are 0.71, 0.74, and 0.69 Å, respectively, for Kv1.1–ShK, Kv1.2–ShK, and Kv1.3–ShK. The standard binding free energy of ShK is determined from

$$\Delta G_b = -k_B T \ln(K_{eq} C_0) \qquad (2)$$

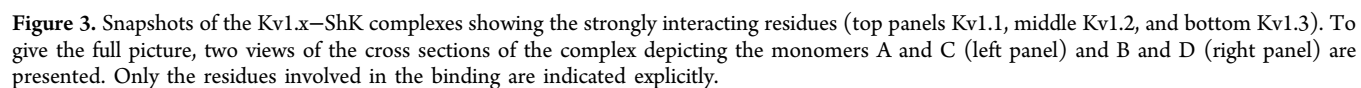where C_0 is the standard concentration of 1 M/L (i.e., $1/C_0 = 1661$ Å^3).

■ RESULTS AND DISCUSSION

Characterization of the Kv1.x–ShK Complexes. Snapshots of the equilibrated Kv1.x–ShK complexes are shown in Figure 3. In order to show all the residues involved in binding, we present two views of the complex depicting the channel monomers A and C, and B and D, separately. A more quantitative description of the strongly interacting residues is provided in Table 2, which shows the average atom–atom distances obtained from 5 ns of unrestrained MD simulations for each complex. Although not apparent from the rmsd calculations (the backbone rmsd of ShK with respect to the NMR structure is 2.4, 2.3, and 2.2 Å when in complex with KV1.1, 1.2 and 1.3, respectively, while the bulk value is 2.2 Å), binding of ShK does cause some small changes in its structure. The most important one occurs in the Kv1.1–ShK complex where the K18(O)–R24(N$_1$) distance increases from 3 Å to about 5 Å, presumably triggered by the E353–K18 coupling. In the other two complexes, K18 and R24 are not involved in any interactions with the channel residues, and the K18–R24 bond remains intact. In the case of Kv1.2–ShK, the T6–F27 H-bond is broken upon binding, and in Kv1.3–ShK, the D5–K30 bond is broken. But these do not appear to be directly linked to the binding of any particular residues in ShK. We stress that once ShK unbinds all three bonds are restored.

We use the results in Figure 3 and Table 2 to validate the Kv1.3–ShK complex, for which there are ample mutagenesis data. Because the interpretation of the double-mutation experiments are model dependent, we prefer to use the alanine scanning results for this purpose.[27] In this study, mutation of R24 in ShK was found to have the strongest effect on binding, followed closely by H19, S20, K22, and Y23. Those having an intermediate effect include R11, T13, M21, L25, F27, and R29. Here the R24A result seems puzzling because the R24 side chain makes a bond with K18 and is not in a position to make any contacts with the channel residues. To understand this experimental result, we have performed MD simulations of the R24A mutant ShK in bulk. The absence of the K18–R24 bond is observed to cause a shape change in the mutant ShK with the two helices moving away from each other by about 2 Å, and concurrent changes occurring in side chain orientations. Thus, the R24A result appears to be an allosteric effect rather than loss of a charge contact.

Comparing the rest of the experimental results with those in Table 2, we find that H19, S20, K22, and Y23 are involved in
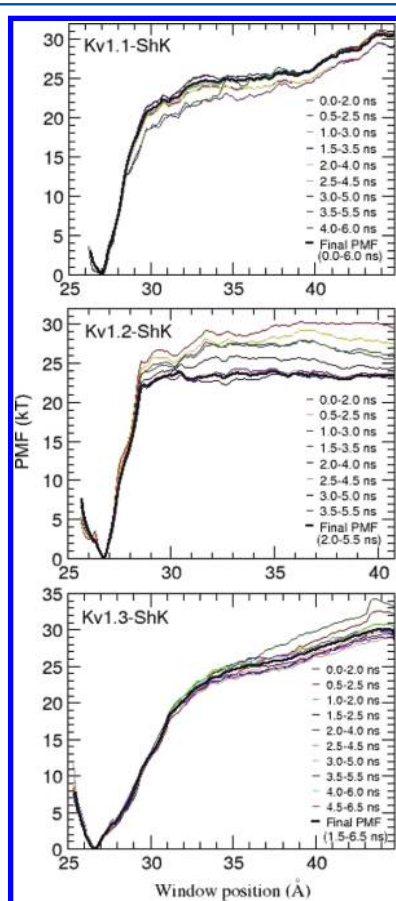
Figure 3. Snapshots of the Kv1.x−ShK complexes showing the strongly interacting residues (top panels Kv1.1, middle Kv1.2, and bottom Kv1.3). To give the full picture, two views of the cross sections of the complex depicting the monomers A and C (left panel) and B and D (right panel) are presented. Only the residues involved in the binding are indicated explicitly.

charge interactions with the channel residues at contact distances, and thus they are expected to be strongly coupled.

Further evidence for this will be provided in Figure 9 when we discuss the dissociation of ShK from Kv1.3. Among the six

4816

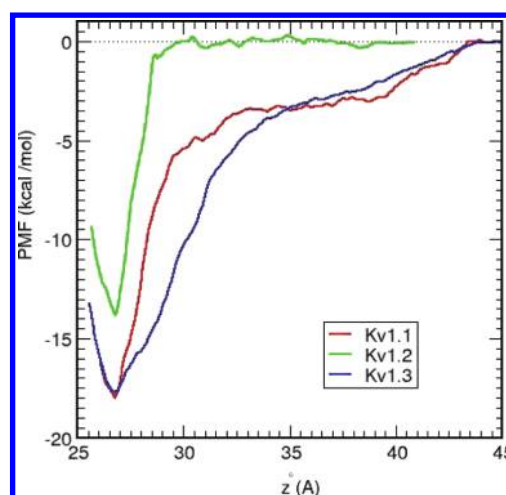dx.doi.org/10.1021/jp300639x | *J. Phys. Chem. B* 2012, 116, 4812−4822
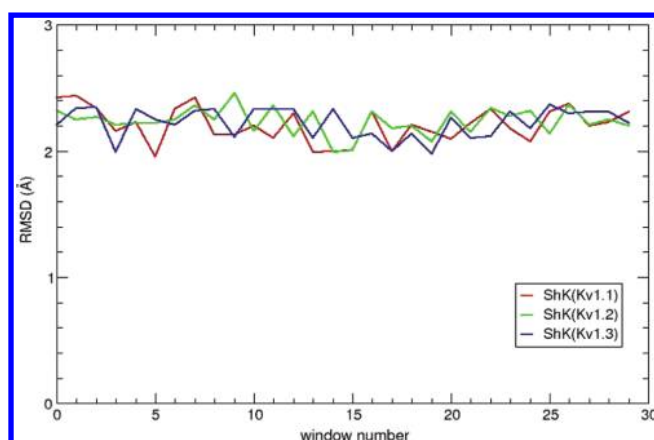
Figure 4. Average rmsd of the ShK backbone atoms with respect to the NMR structure obtained at each window position in the umbrella sampling simulations. The three curves show the results obtained from the Kv1.1−ShK (red), Kv1.2−ShK (green), and Kv1.3−ShK (blue) umbrella simulations.

Figure 6. Comparison of the PMFs obtained from the umbrella sampling simulations for the unbinding of ShK from the Kv1.1, Kv1.2, and Kv1.3 channels. The binding site is at about 27 Å from the COM of the channels.

**Table 3. Comparison of Binding Free Energies for the Three Kv1.x−ShK Complexes**[a]

complex	ΔG_{well}	ΔG_b(PMF)	ΔG_b(expt)
Kv1.1−ShK	−18.0	−14.3 ± 1.1	−14.7 ± 0.1
Kv1.2−ShK	−13.8	−10.1 ± 1.1	−11.0 ± 0.1
Kv1.3−ShK	−17.8	−14.2 ± 1.2	−14.9 ± 0.1

[a]The well depths of the PMFs are shown in the second column. The absolute binding free energy determined from the PMFs (third column) are compared to the experimental values obtained from the dissociation constants.[10] Errors in ΔG_b(PMF) are estimated from the block data analysis of the PMF data. All energies are in kcal/mol.

Figure 5. Convergence study of the Kv1.x−ShK PMFs. To avoid large fluctuations in PMFs, we use a large sampling size (2 ns), which is slided in 0.5 ns steps over the range of the data. In Kv1.3, the final PMF is determined from the last 5 ns of data, around which the individual PMFs are seen to fluctuate.

residues which have an intermediate effect, two are seen to be involved in hydrophobic interactions (M21 and F27), and another two in weaker charge interactions (R11 and R29). Here the H404(C)−F27 coupling is of particular interest because it provides experimental evidence for the H404−D402 cross-linking pattern shown in Figure 1. If all the H404 side

chains were involved in cross-linking, such a coupling would not have been possible, and F27 would be left orphaned. The average N−O distance for R29 is about 10 Å, which clearly indicates a weaker interaction. However, the N−O distance for R11 is 3.5 Å, and it is not readily obvious why the R11−D402 coupling does not produce a stronger interaction. Again, the reason will become clear when we discuss the dissociation of ShK in Figure 9.

We do not see any direct coupling between the channel residues and T13 and L25. Again, the T13 and L25 results may be due to a weaker allosteric effect. The only interaction in Table 2 that is not seen in experiments is R1, which appears to have an intermediate charge interaction with D376. However, in a crowded interface, proximity is not always the best measure of the strength of an interaction, and one needs to look at other quantities. As will be shown in the discussion of Figure 9, D376−R1 is, in fact, one of the weakest interactions.

Correct modeling of the H404 side chains has been instrumental in obtaining the Kv1.3−ShK complex structure that is consistent with the mutagenesis experiments.[27] To make this point clear, we briefly compare our results with those of Chen et al.,[24] where this was not fulfilled. In the complex structure obtained by Chen et al. (Figure 3 in ref 24) ShK has an extremely off-axis position in contrast to our complex where ShK occupies a central position (Figure 3, bottom). This off-axis position of ShK enables a strong charge contact between R11 and the remote D386 residue on the pore helix, which is not seen either in the mutagenesis experiments or in our
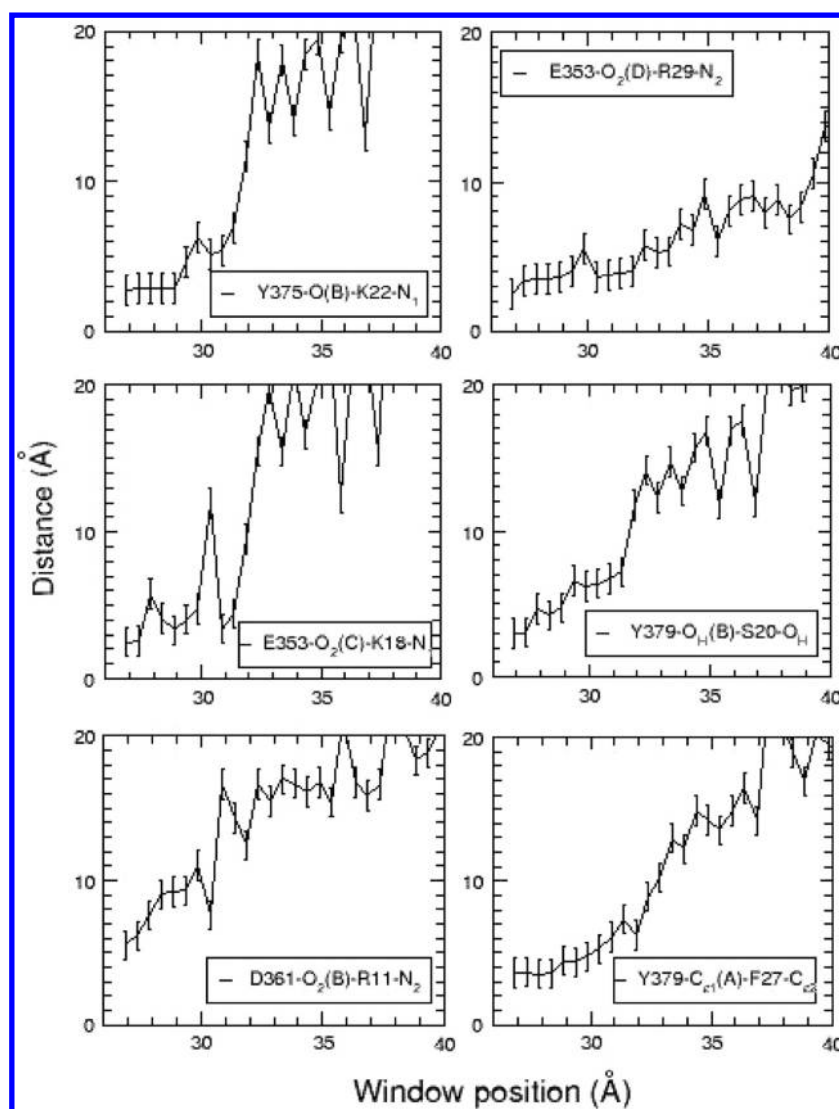
Figure 7. Average distance between the interacting pairs of ShK and Kv1.1 plotted as a function of the window position. All the pairs identified in Table 2 are considered. The trajectory data are taken from the umbrella sampling simulations that have been used in the construction of the final PMFs in Figure 6. Error bars indicate one standard deviation.

complex structure (note that in rat Kv1.3 used in ref 24 this residue corresponds to D433). Besides the pore inserting K22, none of the strongly coupled ShK residues found in the mutagenesis experiments[27] have been identified in the complex structure of Chen et al.[24]

There are no mutagenesis data for the other two complexes, so validation of those models will be based on comparison of the binding free energies. Here we contrast their binding modes with that of Kv1.3−ShK. From Table 1, two important differences between Kv1.1 and 1.3 are the replacement of S378 with E353 and H404 with Y379. As explained in Methods, the bulky Y379 side chains are not involved in cross-linking and prevent S20 and Y23 making H-bonds with the corresponding G376 residues in Kv1.1. Thus, a new interface is formed where (apart from the trivial Y375−K22) only Y379−F27 is retained from the Kv1.3−ShK complex. The lost contacts are compensated by K18 and R29 making charge contacts with the E353 residues in the turret that have replaced S378. Going from Kv1.1 to Kv1.2, E353 is replaced by D355 and Y379 by V381. Thus, one may expect the binding modes in Kv1.1 and Kv1.2 to be similar but inspection of Table 2 shows that two

important contacts in Kv1.1, namely, K18 and S20, are missing in the Kv1.2 complex. Lack of K18 contact is presumably due to the shortness of the prospective partner D355(C), and S20 is prevented from making any H-bonds with the channel residues by the bulky V381 side chains around the filter periphery.

Umbrella Sampling Simulations and PMFs of ShK. For each Kv1.x−ShK complex, umbrella sampling MD simulations are performed as described in Methods. An outstanding issue in PMF calculations of peptides is whether the peptide structure is distorted by the umbrella forces, which could introduce simulation artifacts in the calculation of the binding free energies.[21,22] As discussed earlier, ShK has extra bonds making it quite stable, and therefore it is expected to preserve its shape during the umbrella sampling simulations. This is confirmed by the backbone rmsd calculations of ShK at each umbrella window along the reaction coordinate (Figure 4), which changes little from the bulk value of 2.2 Å in all three cases. Moreover, the structures of ShK in the last umbrella windows are very similar to the NMR structure in all cases with all the bonds preserved. This last point is important because, as
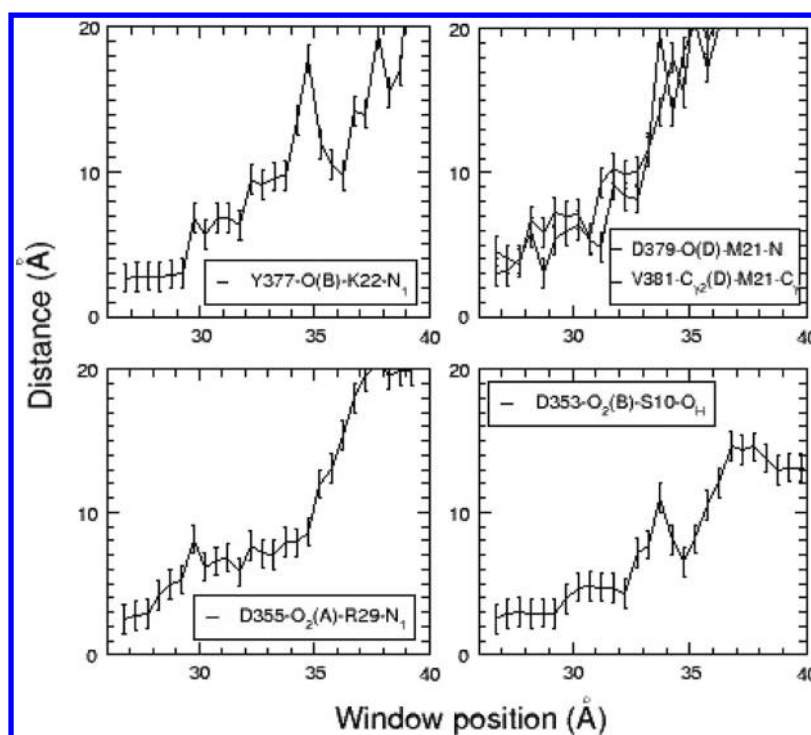
4818

dx.doi.org/10.1021/jp300639x | J. Phys. Chem. B 2012, 116, 4812−4822

Figure 8. Same as for Figure 7 but for the Kv1.2−ShK complex.

discussed above, one of the bonds is affected upon binding of ShK to the channels.

A second issue is whether there are sufficient overlaps between the neighboring windows. From previous studies, a minimum of 3% overlap is required for a stable PMF.[22] Analysis of the initial sampling with 0.5 Å spaced windows indicates that this condition is not satisfied for several windows (e.g., window numbers 6 and 7 in Kv1.1). We have inserted extra windows in those positions to resolve the inadequate overlap problem. Finally, convergence of PMFs is much slower for peptides compared to small, rigid ligands, and extra caution needs to be exercised to ensure that the system has been sampled sufficiently. We have extended umbrella sampling simulations until we have been assured of the convergence of each PMF. Several representations of the PMF data can be used to check the convergence of PMF from simple block data analysis to sliding windows over the range of available data. Here we present the results of the latter method because the results are smoother but we have also used block data analysis in deciding how much data needs to be dropped for equilibration. Convergence studies of the ShK PMFs for unbinding from Kv1.1, 1.2, and 1.3 are shown in Figure 5. We briefly describe the Kv1.3 case as it is of most interest. Each umbrella window is simulated for 6.5 ns, and 10 PMFs are constructed by sliding a 2 ns window over the 6.5 ns of data. The first three PMFs monotonically decrease while the following ones fluctuate around a baseline, which is taken as a sign of convergence. We, therefore, drop the first 1.5 ns of data for equilibration and determine the final PMF from the last 5 ns. In Kv1.1, the initial PMFs do not show any monotonic trend and already fluctuate around a baseline. Therefore, the final PMF is constructed using all the data. In Kv1.2, a downward trend is observed in the initial PMFs. Using the block data analysis results as an additional guide, the first 2 ns of data are dropped for equilibration and the final PMF is constructed from the last 3.5 ns of data.

The final PMFs for each complex are shown in Figure 6, and the absolute binding free energies determined from the PMFs are presented in Table 3 together with the corresponding experimental values. The calculated binding free energies are seen to reproduce the experimental values within the chemical accuracy of 1 kcal/mol in all three cases. Using a similar methodology, we have previously reproduced the binding free energy for the KcsA*−charybdotoxin complex,[22] where the experimental structure of the complex is available.[20] Thus, the success of the present binding free energy calculations gives strong support for the accuracy of the Kv1.x−ShK complex models employed in these calculations.

Conversely, if the complex structure is wrong, then there should be a large discrepancy between the calculated and experimental binding free energies. Despite using a wrong structure for the Kv1.3−ShK complex, a reasonable agreement was obtained for the dissociation constant in ref 24 (a K_d value of 0.17 nM was obtained to be compared with the established experimental value of 0.011 nM[10]). One would have expected a larger discrepancy in the binding free energy than 1.6 kcal/mol implied by this comparison. Indeed, comparison of the PMFs for unbinding of ShK from Kv1.3 (Figure 4 in ref 24 and Figure 6 here) shows that the former is much shallower and has a shorter range indicating a weaker interaction. For example, the well depth of the PMF is −14.6 kcal/mol in ref 24 whereas we obtain −17.8 kcal/mol, which should translate to a larger error in the dissociation constant. The reason it has not is because they used an effective radius of 8 Å for the COM motion of ShK in eq 1, whereas the value estimated from the rmsd of COM of ShK is about 0.7 Å. Thus, the cross-sectional area is overestimated by a factor of 130 and hence the dissociation constant is underestimated by the same factor. Using the correct value of radius would have resulted in a K_d value of 22 nM.

Despite having rather different binding modes, the ShK PMFs for Kv1.1 and Kv1.3 (Figure 6) are quite similar with
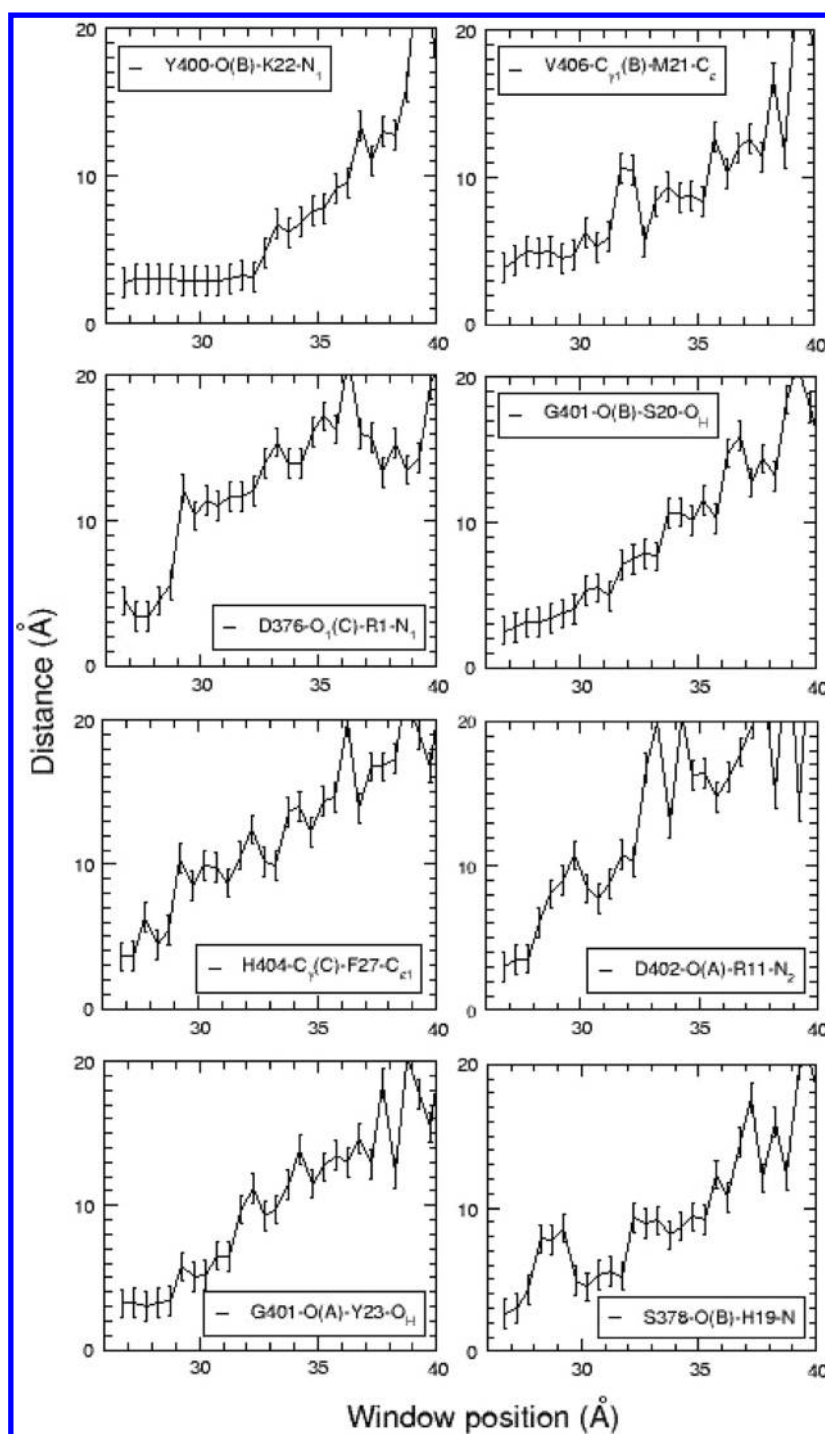
Figure 9. Same as for Figure 7 but for the Kv1.3−ShK complex.

almost the same well depth and binding energies (Table 3). This indicates that the peripheral H-bonds that are lost when going from Kv1.3 to Kv1.1 are fully compensated by the charge contacts gained in the turret region of Kv1.1. As one would expect from the comparison of the Kv1.1−ShK and Kv1.2−ShK complexes above, the affinity of ShK to Kv1.2 is substantially reduced relative to Kv1.1 due to loss of a charge contact. An interesting observation is the lack of long-range electrostatic interactions in the Kv1.2−ShK PMF, which is a prominent feature of the other PMFs. In order to provide a better interpretation of the PMF results and also get a better understanding of the unbinding process, it is necessary to

analyze the individual umbrella windows, which we consider next.

Analysis of the Unbinding Process. The contact pair distances presented in Table 2 gives an idea about the channel and toxin residues involved in the binding but it is difficult to assess their relative strength in such a complex environment. Valuable insights in this regard can be gained by analyzing how the pair distances change as the toxin is pulled out of the binding pocket. Persistence of a contact while the toxin COM is pulled out indicates a strong interaction while increasing of the pair distance proportionally with the toxin COM distance signals a weak interaction. To this end, we calculate the average

pair distances for the pairs listed in Table 2 in each window of the umbrella sampling simulations. The results for the three Kv1.x−ShK complexes are shown in Figures 7, 8, and 9.

Inspection of Figure 7 shows that the E353−R29 interaction is by far the strongest one in the Kv1.1−ShK complex, with R29 keeping contact longest and remaining in the vicinity of the channel much longer than the others. At the opposite end, those involving R11 and S20 are the weakest ones as they exhibit no persistence at all. The remaining three (K18, K22, and F27) are of intermediate strength, keeping contact up to about $z = 30$ Å and then rapidly detaching. This explains the sharp shoulder observed in the corresponding PMF around $z = 30$ Å (Figure 6). The slow rise in the PMF after this point is due to the long-range electrostatic interactions emanating mainly from R29. The pair distances for the Kv1.2−ShK complex (Figure 8) show that all the contacts are lost by $z = 30$ Å. Unlike in Kv1.1, R29 detaches quickly in this case, which may be precipitated by the shorter D side chain coupled to R29. Thus, there are no strong charge interactions left after $z = 30$ Å, which provides an explanation for the flatness of the Kv1.2−ShK PMF after that point.

Dissociation of ShK from Kv1.3 follows a path similar to that from Kv1.1 but it is much smoother (Figure 9). In this case, K22 provides the strongest interaction, its contact with Y400 persisting for almost 6 Å from the binding pocket. The next four in the persistence scale are those involving H19, S20, M21, and Y23, which keep contact for about 4 Å. These five residues match the top five residues identified in the alanine scanning experiments.[27] The remaining three residues (R1, R11, and F27) detach within 1−2 Å of pulling, and hence are relatively weaker interactions. Again this correlates well with the alanine scanning data. The quick departure of the R1 and R11 side chains indicates that they are in high-energy conformations in the bound complex and require only a small shift in the ShK position to detach. Similarly, the H404 side chain is normally buried in the protein, and it has to assume a higher energy conformation in order to make contact with F27. The relative smoothness of the pair distances is reflected in the more gradual rise of the PMF in Kv1.3 compared to Kv1.1 (Figure 6). The turning point in the PMF is at about $z = 33$ Å, which coincides with the detachment of K22—the last contact. After that point, the PMF rises slowly due to the electrostatic interactions, with K22 making the main contribution.

CONCLUSIONS

Computer simulations of biomolecules have been advancing rapidly in recent years both in terms of simulation times and accuracy of the results. In several areas, they have become indispensable tools complementing the available experimental methods. One such area is the determination of protein complex structures, which is notoriously difficult to achieve using experimental methods. Combination of the docking programs with free energy MD simulations provides an alternative method, which has been successfully applied to protein−ligand complexes in the past.[14] Here we have extended this method to binding of a toxin peptide to Kv1 potassium channels. Compared to typical chemical compounds, which are small and relatively rigid, treatment of the larger and more flexible peptides poses a more challenging computational problem. Nevertheless, as shown in this study, such an approach is feasible and one can obtain accurate models of protein−peptide complexes. We stress that validation of the complex models by comparing their predictions with available

experimental data is essential for establishing their reliability. We have used the binding free energies for this purpose, which are uniformly available, and also the mutagenesis data in the case of Kv1.3−ShK complex. The level of agreement is quite good in all cases, lending a strong support for the accuracy of the Kv1.x−ShK complexes constructed in this study.

The main motivation for this study comes from development of ShK and its analogues as an immunosuppressant drug candidate. Many analogues of ShK have been developed in the past decade in order to improve their selectivity for Kv1.3 over Kv1.1, which is essential for their use as a therapeutic drug. The molecular models of the Kv1.x−ShK complexes constructed here will be very useful in this endeavor. We have shown that the surface residues near the filter, Y379 (Kv1.1), V381 (Kv1.2), and H404 (Kv1.3) play a critical role in determining the binding mode of ShK. The cross-linking of H404−D402 residues in Kv1.3 allows ShK come closer to the filter and make H-bonds with the nearby residues. Such a cross-linking does not occur in Kv1.1 and Kv1.2, and the bulky Y379 and V381 side chains prevent ShK making similar H-bonds. This is compensated by charge interactions in the turret region in Kv1.1 but not in Kv1.2, which explains the lower affinity of ShK to Kv1.2. The differences in the binding modes documented in Table 2 readily suggest a few mutations that could increase the selectivity of ShK for Kv1.3 over Kv1.1. Two obvious candidates are K18 and R29. We hope to pursue mutations of these residues as well as other ShK analogues proposed from experimental studies in future work.

■ AUTHOR INFORMATION

Corresponding Author
*E-mail: serdar@physics.usyd.edu.au.

Notes
The authors declare no competing financial interest.

■ REFERENCES

(1) Hille, B. *Ionic Channels of Excitable Membranes*, 3rd ed.; Sinauer Associates: Sunderland, MA, 2001.
(2) Ashcroft, F. M. *Ion Channels and Disease: Channelopathies*; Academic Press: San Diego, CA, 2000.
(3) Wulff, H.; Zhorov, B. S. *Chem. Rev.* **2008**, *108*, 1744−1773.
(4) Wulff, H.; Castle, N. A.; Pardo, L. A. *Nat. Rev. Drug Disc.* **2009**, *8*, 982−1001.
(5) Wulff, H.; Calabresi, P. A.; Allie, R.; Yun, S.; Pennington, M.; Beeton, C.; Chandy, K. G. *J. Clin. Invest.* **2003**, *111*, 1703−1713.
(6) Beeton, C.; Wulff, H.; Standifer, N. E.; Azam, P.; Mullen, K. M.; Pennington, M. W.; Kolski-Andreaco, A.; Wei, E.; A. Grino, A.; Counts, D. R.; et al. *Proc. Natl. Acad. Sci. U.S.A.* **2006**, *103*, 17414−17419.
(7) Cahalan, M. D.; Chandy, K. G. *Immunol. Rev.* **2009**, *231*, 59−87.
(8) Castaneda, O.; V. Sotolongo, A; M. Amor, R.; Stocklin, A. J.; Anderson, A. L.; Harvey, A.; Engstrom, C.; Wernstedt; Karlsson., E. *Toxicon* **1995**, *33*, 603−613.
(9) Norton, R. S. *Toxicon* **2009**, *54*, 1075−1088.
(10) Kalman, K.; Pennington, M. W.; Lanigan, M. D.; Nguyen, A.; Rauer, H.; Mahnir, V.; Paschetto, K.; Kem, W. R.; Grissmer, S.; Gutman, G. A. *J. Biol. Chem.* **1998**, *273*, 32697−32707.

4821

dx.doi.org/10.1021/jp300639x | *J. Phys. Chem. B* 2012, 116, 4812−4822

(11) Norton, R. S.; Pennington, M. W.; Wulff, H. *Curr. Med. Chem.* **2004**, *11*, 3041−3052.

(12) Chi, V.; Pennington, M. W.; Norton, R. S.; Tarcha, E. J.; Londono, L. M.; Sims-Fahey, B.; Upadhyay, S. K.; Lakey, J. T.; Iadonato, S.; Wulff, H.; et al. *Toxicon* **2011**, *59*, 529−546.

(13) Pennington, M. W.; Beeton, C.; Galea, C. A.; Smith, B. J.; Chi, V.; Monaghan, K. P.; Garcia, A.; Rangaraju, S.; Giuffrida, A.; Plank, D.; et al. *Mol. Pharmacol.* **2009**, *75*, 762−773.

(14) Alonso, H.; Bliznyuk, A. A.; Gready, J. E. *Med. Res. Rev.* **2006**, *26*, 531−568.

(15) Gilson, M. K.; Zhou, H. X. *Annu. Rev. Biophys. Biomol. Struct.* **2007**, *36*, 21−42.

(16) Nervall, M.; Hanspers, P.; Carlsson, J.; Boukharta, L.; Aqvist, J. *J. Med. Chem.* **2008**, *51*, 2657−2667.

(17) Deng, Y.; Roux, B. *J. Phys. Chem. B* **2009**, *113*, 2234−2246.

(18) Christ, C. D.; Mark, A. E.; van Gunsteren, W. F. *J. Comput. Chem.* **2010**, *31*, 1569−1582.

(19) Steinbrecher, T.; Labahn, A. *Curr. Med. Chem.* **2010**, *17*, 767−785.

(20) Yu, L. P.; Sun, C. H.; Song, D. Y.; Shen, J. W.; Xu, N.; Gunasekera, A.; Hajduk, P. J.; Olejniczak, E. T. *Biochemistry* **2005**, *44*, 15834−15841.

(21) Chen, P. C.; Kuyucak, S. *Biophys. J.* **2009**, *96*, 2577−2588.

(22) Chen, P. C.; Kuyucak, S. *Biophys. J.* **2011**, *100*, 2466−2474.

(23) Khabiri, M.; Nikouee, A.; Cwiklik, L.; Grissmer, S.; Ettrich, R. *J. Phys. Chem. B* **2011**, *115*, 11490−11500.

(24) Chen, R.; Robinson, A.; Gordon, D.; Chung, S. H. *Biophys. J.* **2011**, *101*, 2652−2660.

(25) Dominguez, C.; Boelens, R.; Bonvin, A. *J. Am. Chem. Soc.* **2003**, *125*, 1731−1737.

(26) de Vries, S.; J.; van Dijk, A. D. J.; Krzeminski, M.; van Dijk, M.; Thureau, A.; Hsu, V.; Wassenaar., T.; Bonvin, A. M. J. J. *Proteins* **2007**, *69*, 726−733.

(27) Rauer, H.; Pennington, M.; Cahalan, M.; Chandy, K. G. *J. Biol. Chem.* **1999**, *274*, 21885−21892.

(28) Long, S. B.; Campbell, E. B.; MacKinnon, R. *Science* **2005**, *309*, 897−903.

(29) Long, S. B.; Tao, X.; Campbell, E. B.; MacKinnon, R. *Nature* **2007**, *450*, 376−382.

(30) Humphrey, W.; Dalke, A.; Schulten, K. *J. Mol. Graphics* **1996**, *14*, 33−38.

(31) Bastug, T.; Kuyucak, S. *Biophys. J.* **2009**, *96*, 4006−4012.

(32) Bastug, T.; Kuyucak, S. *Biophys. J.* **2011**, *100*, 629−636.

(33) Chen, P. C.; Kuyucak, S. *Toxins* **2012**, *4*, 110−138.

(34) Tudor, J. E.; Pallaghy, P. K.; Pennington, M. W.; Norton, R. S. *Nat. Struct. Biol.* **1996**, *3*, 317−320.

(35) Patra, S. M.; Bastug, T.; Kuyucak, S. *J. Phys. Chem. B* **2007**, *111*, 11303−11311.

(36) Phillips, J. C.; Braun, R.; Wang, W.; Gumbart, J.; Tajkhorshid, E.; Villa, E.; Chipot, C.; Skeel, R. D.; Kale, L.; Schulten, K. *J. Comput. Chem.* **2005**, *26*, 1781−1802.

(37) MacKerell, A. D., Jr.; Bashford, D.; Bellott, M.; Dunbrack, R. L., Jr.; Evanseck, J. D.; Field, M. J.; Fisher, S.; Gao, J.; Guo, H.; Ha, S.; et al. *J. Phys. Chem. B.* **1998**, *102*, 3586−3616.

(38) MacKerell, A. D.; Feig, M.; Brooks, C. L. *J. Comput. Chem.* **2004**, *25*, 1400−1415.

(39) Kumar, S.; Bouzida, D.; Swensen, R. H.; Kollman, P. A.; Rosenberg, J. M. *J. Comput. Chem.* **1992**, *13*, 1011−1021.